

Contents lists available at ScienceDirect

Journal of the Mechanical Behavior of Biomedical Materials

journal homepage: www.elsevier.com/locate/jmbbm



Research paper



Axially- and torsionally-polarized radially converging shear wave MRE in an anisotropic phantom made via Embedded Direct Ink Writing

Martina Guidetti ^{a,*}, Marco Andrea Zampini ^c, Yizhou Jiang ^b, Chiara Gambacorta ^a, Joshua P. Smejkal ^a, Joseph Crutison ^a, Yayue Pan ^b, Dieter Klatt ^a, Thomas J. Royston ^a

- a University of Illinois at Chicago, Richard and Loan Hill Department of Bioengineering, University of Illinois at Chicago, Chicago, IL 60607, USA
- b University of Illinois at Chicago, Department of Mechanical and Industrial Engineering, University of Illinois at Chicago, Chicago, IL 60607, USA
- ^c MR Solutions Ltd, Ashbourne House, Old Portsmouth Rd, Guildford, United Kingdom

ARTICLE INFO

Keywords: Magnetic Resonance Elastography Complex shear moduli Tabletop MRI Phantom design Additive manufacturing Embedded Direct Ink Writing

ABSTRACT

Magnetic Resonance Elastography (MRE) is a non-invasive imaging method to quantitatively map the shear viscoelastic properties of soft tissues. In this study, Embedded Direct Ink Writing is used to fabricate a muscle mimicking anisotropic phantom that may serve as a standard for imaging studies of anisotropic materials. The technique allowed us to obtain a long shelf life silicone-based phantom expressing transverse isotropic mechanical properties. Another goal of the present investigation is to introduce a torsionally-polarized, radially-converging shear wave actuation method for MRE. The implemented design for this novel setup was first validated via its application to isotropic and homogeneous gelatin phantoms. Then, a comparison of the resulting complex wave images from axially- and torsionally-polarized MRE on the developed anisotropic phantom and on a skeletal muscle murine sample is presented, highlighting the value of using multiple actuation and motion encoding polarization directions when studying anisotropic materials.

1. Introduction

Dynamic elastography methods - based on optical, ultrasonic, and magnetic resonance imaging modalities - are being used for quantitatively mapping the shear viscoelastic properties of biological tissue. which are often altered by disease and injury. Optical methods span from early work using stroboscopy (Von Gierke et al., 1952) to more recent, higher resolution methods using optical coherence tomography (Liang and Boppart, 2009; Larin and Sampson, 2017) or laser Doppler vibrometry (Khan et al., 2018) to estimate the material properties at or near the surface, such as for the skin or cornea. Ultrasound (US)-based elastography has been implemented in a number of different ways using continuous or transient excitation (Yamakoshi et al., 1990; Parker et al., 1990; Dutt et al., 2000; Deffieux et al., 2011; Wang et al., 2013; Sarvazyan et al., 2011). Magnetic resonance elastography (MRE), introduced in 1995 (Muthupillai et al., 1995), is replacing biopsy as the gold standard for non-invasive diagnosis and staging of liver fibrosis (Ajmera et al., 2020). In addition, MRE has displayed promising results for the detection and monitoring of neuromuscular and neurodegenerative diseases (Oin et al., 2014; Bensamoun et al., 2007; Ringleb et al., 2007; Botanlioglu et al., 2013; McCullough et al., 2011; Lieber and Fridén, 2000; Sack et al., 2013; Garmirian et al., 2009), involving highly anisotropic tissues, such as skeletal muscle (Basford et al., 2002)

and white matter in the brain (Schmidt et al., 2018), which present different elastic properties along and across the fibers (Kalra et al., 2019). This makes interpretation of MRE measurements more difficult, but also offers the prospect of obtaining new clinically-relevant information when wave motion is provided in multiple directions in order to capture the direction-dependent properties of the tissue (Anderson et al., 2016; Habe et al., 2020).

Implementation of biomimetic phantoms has facilitated improvements in MRE (Muthupillai et al., 1995; Nguyen et al., 2014; Cao et al., 2017). These phantoms can be fabricated through a variety of methods and materials, including water-based (Amador et al., 2011; Quan et al., 1993; Doyley et al., 2001; Hall et al., 1997; Doyley et al., 2001; Hall et al., 1997; Guidetti et al., 2019; Hamhaber et al., 2003; Manduca et al., 2001; Zell et al., 2007; Plewes et al., 2000; Madsen et al., 2005; Ringleb et al., 2005; Pavan et al., 2010) and polymeric-based (Mori et al., 1997; Zell et al., 2007; Madsen and Frank, 1997; Oudry et al., 2009; Brinker and Klatt, 2016; Brinker et al., 2018) materials. However, most of these phantoms possess degradable characteristics, complicating their standardization and use as a means of validation (Mun et al., 2013). Embedded Direct Ink Writing (EDIW), an Additive Manufacturing (AM) method, has been of great interest in

^{*} Correspondence to: 5718 N Winthrop Ave, Chicago, IL, 60660, USA. E-mail address: mguide2@uic.edu (M. Guidetti).

the field of biomaterials (Muth et al., 2014; Truby et al., 2018; Noor et al., 2019): unlike conventional Direct Ink Writing processes, with EDIW materials are extruded "on the fly" without distinct layer-based support structures, leaving a free-standing three-dimensional structure. The 3D printed structure is constructed within a host material (Muth et al., 2014; Truby et al., 2018) or a removable matrix (Noor et al., 2019). This new manufacturing process overcomes several constraints present in traditional extrusion-based additive manufacturing techniques, including layer construction and support structures for internal cavities.

This paper outlines the development of both an advanced AM technique to obtain durable, silicone-based, transversely isotropic phantoms and a novel torsional MRE actuation system built for a low-cost low-field tabletop MRI system. The anisotropic phantom is then characterized using our torsional system and a standard axial system, which when used serially on the same sample, enable shear wave polarization in 2 orthogonal directions in order to identify both slow and fast shear wave motion that is present in transversely isotropic materials. The same characterization is also applied to isotropic and homogeneous gelatin phantoms. Additionally, serially applied axial and torsional actuation studies are performed on an excised thigh and calf muscle of a mouse.

2. Materials and methods

Three different kinds of samples were prepared: a homogeneous and isotropic gelatin sample at 5% weight per volume (w/v), a silicone-based transverse isotropic phantom, and an excised murine thigh and calf sample. The 5% w/v gelatin solution was poured in the test tube and the experiment was not run until complete solidification and adhesion of the sample to the test tube walls. The matrix of the silicone-based anisotropic phantom was sticky enough to solidly adhere to the test tube walls. The murine muscle sample was kept in place and adhesion to the walls was facilitated using gelatin solution that was poured on the top and bottom of the sample. Each sample was tested with actuation polarized in two orthogonal directions and the corresponding wave images were extracted. For all samples estimation of shear moduli was also conducted.

2.1. Isotropic gelatin fabrication and murine sample preparation

A 5% w/v gelatin solution was prepared by solubilization of Gelatin Powder (IS16003, Lab Grade, Innovating Science $^{\text{m}}$, Aldon Corporation, Avon, NY) in distilled water.

Murine thigh and calf sample was excised from a dissected adult wild-type female B6SJLF1 mice (> 9 months). The animal under consideration was euthanized as part of an authorized protocol for a different study.

An annular incision was made around the distal portion of the lower limb, followed by an incision along the length of the lateral edge of the tibia to expose the muscle. After dissection of the lower gastrocnemius and soleus, another incision was made along the side of the knee joint up to the proximal end of the lower limb, the skin was dissected away to give a clear view of the anatomy. The quadriceps femoris were then probed away from the surrounding musculature and cut directly above the knee and directly below the origin points on the pelvis. All muscles were then placed horizontally inside a test tube used for imaging purposes with the fiber direction being primarily in parallel to the image plane. The test tube was open on both ends and the sample was bounded by gelatin on either sides outside of the imaged region (Yasar et al., 2013). The tissue was then imaged within one hour after excision to limit the amount of degradation and rigor.

2.2. Anisotropic phantom fabrication

The biomimetic muscle structure was fabricated using embedded direct ink process which involves two types of materials: the supporting matrix material and the printed filament material. To the authors' best knowledge, there are no strict requirements for the materials to be used in this process. Many applications have been reported using this technique (Muth et al., 2014; Truby et al., 2018; Grosskopf et al., 2018; Zhao et al., 2020; Zhao and He, 2020). Some preferred common properties of the supporting matrix material and the printed filament material are similar densities, insolubility, etc. First, the gel base matrix material was loaded into a customized aluminum container at room temperature (Fig. 1a and 2a). The design of the uniform muscle fiber bundles in polydimethylsiloxane (PDMS) consists of numerous aligned filaments, as shown in Fig. 1b, 2b and 2c. The diameter and the length of the filament is approximately 200 µm and 20 mm, respectively. The center-to-center distance between the fibers is approximately 250 µm. Second, an array of 40 biomimetic muscle filaments was fabricated by extruding the material through a 200 µm diameter, blunt stainlesssteel dispensing tip at 20 mm/s speed under 5psi air pressure close to the bottom of the aluminum container. Third, the dispensing tip was moved up by 250 µm to fabricate the next array of filaments. This process then continued until the total height of repeating arrays was 20 mm (repeated 80 times). The width of the cylindrical filament W was estimated as:

$$W = 2\sqrt{\frac{Q}{\pi \nu}} \tag{1}$$

where Q $[mm^3/s]$ is the applied flow rate from the dispenser and v [mm/s] is the printing speed.

After fabrication, the gel matrix was heated at 75 °C for 24 h. The heating process both accelerates the solidification of the PDMS filaments and evaporates the majority of the water content within the base gel. Hence, in the vertical direction, the distance between two adjacent filaments slightly decreased, as shown in Fig. 1c. Carbomer and sodium by-products in the gel base matrix were then washed by a water bath. Finally, activated Alumisol Soft Plastic (ASP) was poured over the sample to form the artificial extracellular matrix of the phantom (Figs. 1d and 2d). PDMS and ASP were chosen based on their longevity after activation. Indeed, PDMS is commonly used as a sealing material for wearable electronics and microfluidics fabrication thanks to its durability (Jiang et al., 2019; Kim et al., 2018; Fujii, 2002).

2.2.1. Preparation of the gel base

The matrix used for supporting biomimetic muscle fibers was prepared by adding 0.5 g of Carbomer 940 powder (MakingCosmetics) to deionized water (100ml), followed by stirring (Eurostar 60, IKA) at a 400 rpm until the powder was fully hydrated. The mixture was then degassed by a centrifuge. Afterwards, 0.125M sodium hydroxide was added to the solution until the pH was approximately 6.0, which gave a gel structure. After the biomimetic muscle fibers were finished printing, the gel structure was removed by overnight heating and a water bath.

2.2.2. Preparation of biomimetic muscle fibers

A two-part silicone elastomer (Dow Sylgard 184 known as PDMS) was used for the fabrication of the biomimetic muscle fibers. 10.0 g base, 1.0 g curing agent and 0.5 g purple dye powder for visualization were mixed at 2000 rpm for 5 min at room temperature. The solution was then loaded into a 10cc syringe barrel for printing. Upon the completion of printing, the filaments are transferred to an oven and heated up to 75 °C for 24 h to ensure thorough solidification of the elastomer.

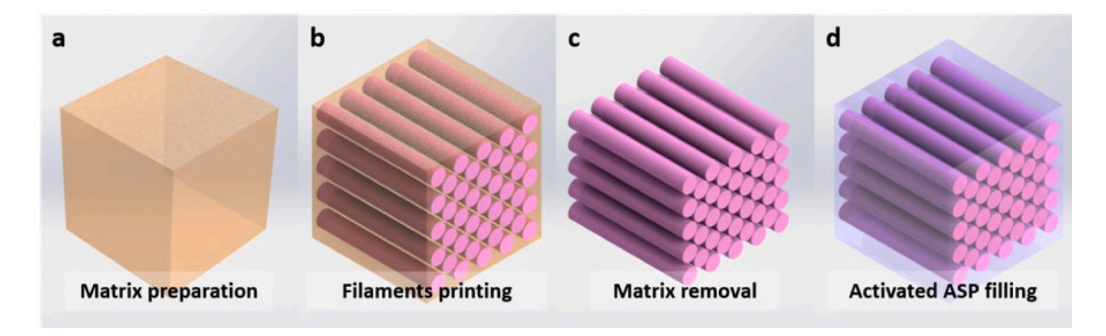


Fig. 1. Design and manufacturing process of the biomimetic muscle tissue. (a) Matrix before printing. (b) Printed uniform PDMS filaments. (c) Removing matrix by heating and water bath. (d) PDMS filaments filled by activated Alumisol Soft Plastic (ASP).

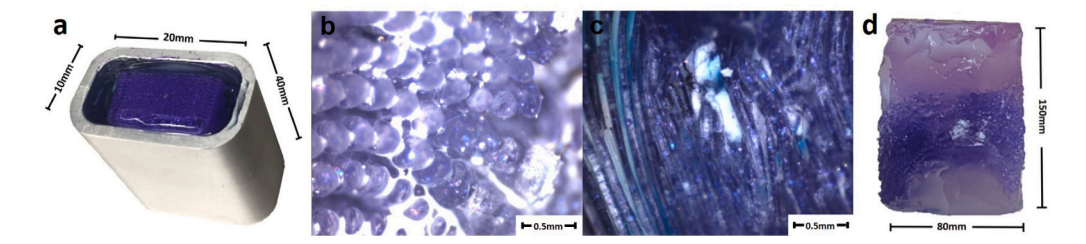


Fig. 2. Manufacturing details of the biomimetic muscle tissue. (a) Gel matrix with printed PDMS filaments. (b) Printed uniform PDMS filaments. (c) Removing matrix by heating and water bath. (d) Final composite anisotropic phantom with Alumisol Soft Plastic (ASP) matrix and PDMS printed filaments.

2.2.3. Preparation of biomimetic muscle matrix

Alumisol Soft Plastic (ASP) was purchased and used as received. It is a translucent heat-activated silicone with very low hardness (30 Shore OO hardness). It was first activated by heating at 160 °C for 30 min. After the printed muscle fibers solidified, and the gel base matrix was removed, the activated liquid ASP was poured into the printing chamber. Solidification was then reached at room temperature.

2.2.4. Phantom manufacturing setup

A modified, commercially available automated dispensing system (E3V, Nordson EFD) was used for manufacturing. Modifications allowed for it to be implemented as an Embedded Direct Ink Writing Printer (Fig. 3). Air pressure and vacuum level were accurately controlled by a dispenser (Ultimus II, Nordson EFD). Filaments were directly written using various stationary blunt syringe tips made of stainless steel (0.20 mm inner diameter, 25.4 mm length, McMaster-Carr). The ink solution was prepared and loaded into a 10cc syringe, which was then mounted onto a carriage that could move in the three spatial directions. The experimental setup also consisted of a pressure controller that regulates the flow rate of the ink, a heated print bed that can be adjusted from 25 °C to 200 °C, and a CCD camera for visually monitoring the distance between the tip of the syringe and the printing surface.

The order of operations for the printing process began by moving the syringe to the starting position set by the controlling software. Upon reaching the starting position, the syringe began traversing and dispensing the ink solution with software-controlled speed and flow rate. The controller was set to turn off the air supply when the print job was complete, in order to stop the ink from dispensing. The controller then would move the syringe away from the finished phantom in order to remove it from the print bed.

2.3. Rheological properties estimation for the inks

Printability was assessed estimating the rheological properties of the inks (PDMS material used to mimick muscle fibers and the hydrogel supportive matrix) using a rotational rheometer (Kinexus Ultra+; Malvern) equipped with a 25 mm diameter plate geometry. The plate

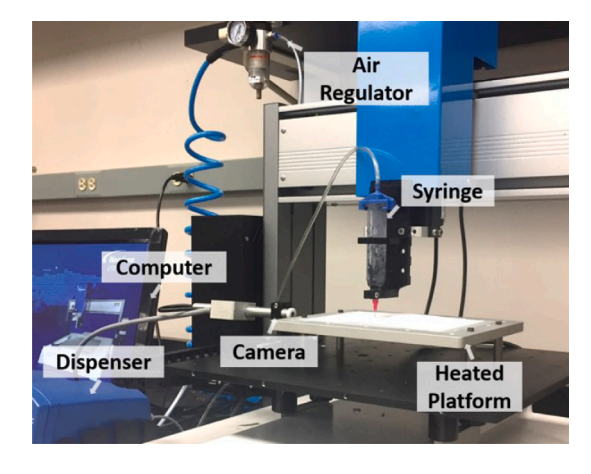


Fig. 3. Direct Ink Writing (DIW) system setup.

geometry is supported by a virtually frictionless air bearing and driven by an ultralow inertia motor, coupled to an ultrahigh precision position encoder. In all experiments, the inks were equilibrated at 25 °C for 15 min before testing. The sample was then loaded into the gap of a fixed substrate and the plate geometry. Herein, the rheological characteristics of the sample can be determined by rotational oscillation, based on the controllable motor torque. The test runs a logarithmically spaced array of shear rates and measures the apparent viscosity with a 25 °C testing temperature for each material.

PDMS demonstrates both shear-thinning and viscoelastic properties, ensuring a high printability in the DIW process with easy extrusion capability and high shape-stability (Smay et al., 2002). On the other hand, by characterizing the storage modulus and loss modulus, we confirm that the prepared hydrogel matrix exhibited solid-like behaviors, providing sufficient supporting for the extruded filament in a three-dimensional configuration (M'barki et al., 2017).

2.4. MRE experimental setup

MRE experiments were performed using a vertical bore (10 mm diameter) tabletop MR scanner (Researchlab, Pure Devices GmbH, Würzburg, Germany) with a 0.587T permanent magnet (MagSpec). The scanner was controlled by a driver console (drivel) and connected to an external gradient amplifier (DC 600).

To induce mechanical excitation of the phantoms for the MRE experiments, two custom-built setups were manufactured with the aim of building a high-inertial, deformation-resistant and durable support structure at a low cost. The first setup implemented a piezoelectric actuator for vertical axial excitation of the phantoms (Fig. 4a). A similar axial excitation system can be found in the studies from Braun et al. (2018) and Ipek-Ugay et al. (2015). The second setup implemented a stepper motor device for torsional excitation in the horizontal plane of the phantoms (Fig. 4b). Both setups were constructed from polycarbonate due to its low relative magnetic permeability, high density and high Young's modulus. The components of both setups were machined from sheets of polycarbonate on a Bridgeport vertical milling machine. After all of the components were machined to specifications, they were chemically bonded using SCIGRIP 4 Acrylic Solvent Cement.

2.5. MRE experiments

The axial actuation was achieved using a piezoelectric driver (PAHL series, model 60/20 by Piezosystem Jena GmbH, Jena, Germany) fed with a sinusoidal oscillating current with a vibration-amplitude dependent voltage (maximum 90V), while the torsional actuation was given by a single shaft bipolar stepper motor with a step angle of 1.8° , a holding torque of 18Ncm, a rated current of 0.8 A and a voltage of 5.4 V with dimensions being $35 \times 35 \times 34$ mm (model Nema 14HS13-0804S by STEPPERONLINE, Jiangning District Nanjing City, China).

In order to proceed with the MRE experiment each sample was placed inside a 8 mm inner diameter glass tube open on both ends so to minimize the effect of the compression waves in the axial direction of the tube. In particular, the anisotropic phantom and the murine samples were positioned with the fibers lying in the cross-sectional plane of the test tube, as described in Guidetti and Royston (2018), in order to generate converging slow and fast shear waves, with axial or torsional actuation, respectively. The tube was then harmonically vibrated, axially or torsionally, with the piezoelectric or stepper motor actuator, respectively, to run multifrequency Spin Echo sequence-based MRE experiments. The combination of the values for the MRE sequence parameters was chosen depending on the modality of actuation with the main parameters being:

- Excitation frequency: 500 to 2000 Hz;
- Motion Encoding Gradient: sinusoidal, duration = 3 ms, amplitude = 0.1 to 0.7T/m;
- Number of phase steps = 8;
- Displacement amplitude = 7 to 36 μm (chosen accordingly to each excitation frequency);
- Acquisition matrix size = 64×64 ;
- Field of view = 10×10 mm;
- Slice thickness = 5 mm;
- Motion encoding directions: vertical for the axial experiment; both horizontal directions for the torsional experiment.

2.6. Data processing and analysis

For each voxel of the MR phase images, a discrete Fourier Transform was applied along the eight samples. Complex waves images were extracted from the first harmonic and scaled by the motion encoding efficiency, for each frequency of excitation, in a single or in two different motion encoding directions for the axially and torsionally-polarized MRE experiment, respectively. The complex wave images in the two different encoding directions, as obtained from the torsionally-polarized

MRE experiment, were combined together in order to compute the complex displacement maps in the θ direction, as defined in the polar coordinate system.

When dealing with transverse isotropic samples, such as in the present work, it is possible to apply the Transformation Elastography theory (Guidetti et al., 2020), which creates isotropic conditions via a geometrical distortion proportional to the level of anisotropy within the material. This allows for conventional inversion algorithms, such as direct inversion (Klatt et al., 2007), to be utilized in computing elastograms. Since direct inversion does not consider boundary effects, we also estimated the shear modulus by fitting the wave profiles with Bessel functions in a closed form expression which accounts for boundary effects (Yasar et al., 2013; Graff, 2012). A limitation of the Bessel fit analytical solution is that it does not consider the resonances dependent on the cylinder height, thus neglecting the effect of finite boundaries on the top and bottom of the cylindrical phantom. Even if this limitation introduces a small amount of error into the theoretical solution for the axial polarization, the error is independent of anisotropy.

For the experimental configuration in which axially-polarized shear waves are generated, only slow shear waves are driven and consequently only the shear anisotropic ratio parameter (and not the tensile anisotropic parameter) comes into play and it defined as (Guidetti and Royston, 2018):

$$\phi = \frac{\mu_{\parallel}}{\mu_{\perp}} - 1 \tag{2}$$

Therefore, the direct inversion algorithm will feature a contraction, y^1 , in the direction of alignment of the fibers, y, that is a function of the shear anisotropic ratio, ϕ , as follows:

$$y^{1} = \frac{y}{\sqrt{1+\phi}} = \frac{y}{\sqrt{\frac{\mu_{\parallel}}{\mu_{\perp}}}} \tag{3}$$

Ultimately the ratio between the long (parallel to the fibers) and the short (perpendicular to the fibers) wavelength – which can be deduced from the elliptical wavefronts – will provide an estimate for the shear anisotropic ratio.

Having obtained isotropy upon transformation, at this point it was possible to apply the direct inversion algorithm to retrieve values for the shear modulus in the perpendicular direction to the fibers. The standard deviation associated to the complex shear modulus was computed from all the values corresponding to the pixels included in the region of interest restricted to a circular central area of 3 mm radius to reduce boundary effects from the calculation. Lastly, the shear modulus in the direction of the fibers was calculated by multiplying the value of the shear modulus in the direction perpendicular to the fibers by the shear anisotropic ratio plus one. This parameter was obtained by calculating the ratio of the wavelength in the direction parallel and perpendicular to the fibers, both for the real and imaginary parts of the wave images, with an automated calculation exploiting the fit_ellipse (Gal, 2020) function in Matlab as shown in Fig. 6.

3. Results and discussion

3.1. Rheological properties for the inks

The PDMS material used for the filament ink exhibited a slight shear thinning behavior during rheological testing. The apparent viscosity decreased from 7.1 Pa s to 5.9 Pa s as the shear rate increased from $0.1s^{-1}$ to $100s^{-1}$, allowing it to be extruded through fine deposition nozzles. Printing was further enabled by its yielding behavior. As shown in Fig. 5, above the shear yield stress (approximately 0.2Pa), its shear storage modulus μ decreased dramatically with increased shear stress, allowing the ink to be printed at low pressures.

The as-prepared matrix showed a strong shear thinning behavior, a moderate shear yield stress (Fig. 5) to accommodate rapid nozzle translation, a relatively high μ (approximately 115 Pa) to support the printed ink filaments without compressing their geometry, and a capability to be cured after printing is done.

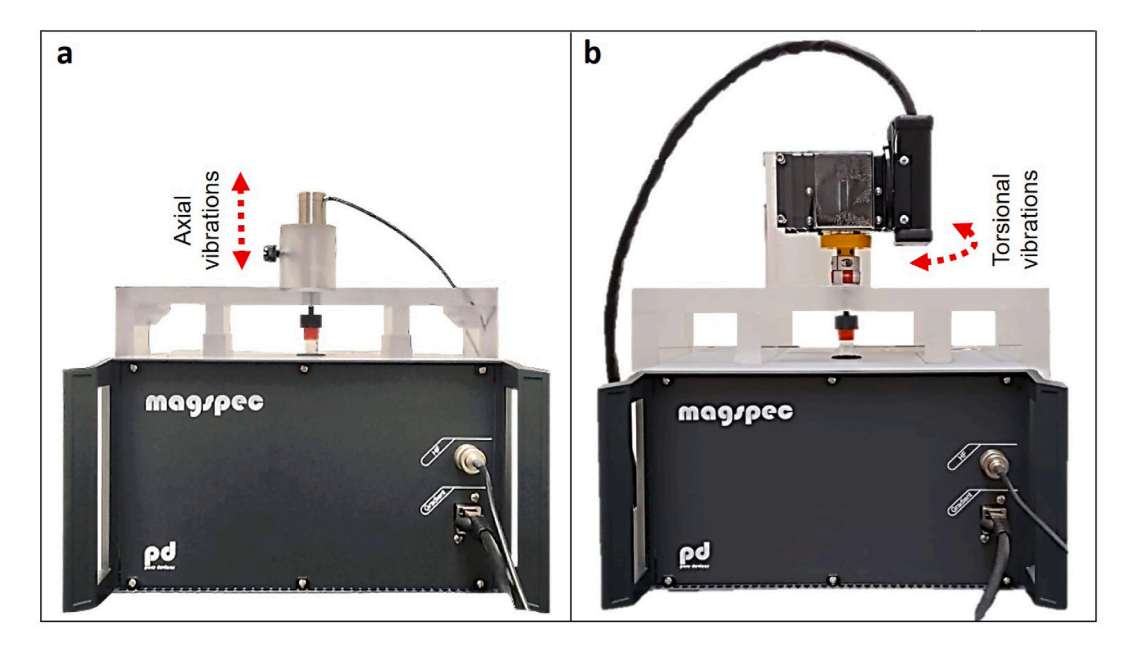


Fig. 4. (a) Picture of the MRE setup for piezoelectric actuator support mounted on the tabletop MRI machine by Pure Devices GmbH, Würzburg, Germany. (b) Picture of the MRE setup for stepper motor actuator support mounted on the tabletop MRI machine by Pure Devices GmbH, Würzburg, Germany.

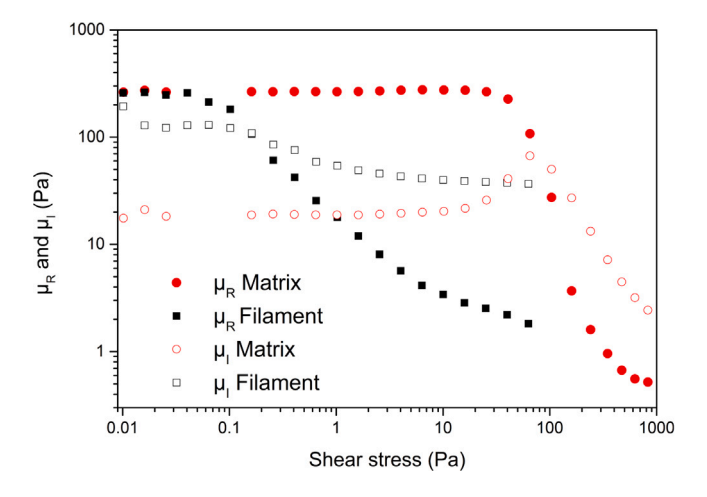


Fig. 5. Rheological properties estimation for printability assessment of the inks. Storage modulus (μ_R) and loss modulus (μ_I) of the PDMS filament fiber (filament ink) and of the hydrogel support matrix as a function of the shear stress measured by the rheometer (shear stress sweep at the default oscillation frequency of 1 Hz).

3.2. MRE experimental results

Both axial and torsional MRE experimental wave images are shown in Fig. 7 for the homogeneous isotropic gelatin sample. The first column contains the axial displacement maps, while the second one corresponds to the θ displacement, respectively obtained from axially and torsionally-polarized MRE experiments at 800 Hz (top row: real part; bottom row: imaginary part). Comparing the images on the two columns, it is possible to notice that the wavefronts are circular as expected from the theory of converging shear waves in bounded homogeneous and isotropic materials. Moreover, the wavelength is constant and equal for both the axially and the torsionally-polarized wave images as expected for an isotropic material and thus validating the implemented torsional MRE setup. Shear modulus was computed upon the application of the direct inversion algorithm (Fig. 8). Shear moduli computed with inversion method based on fitting the wave profiles with closed form solution Bessel equation is provided in Appendix A.

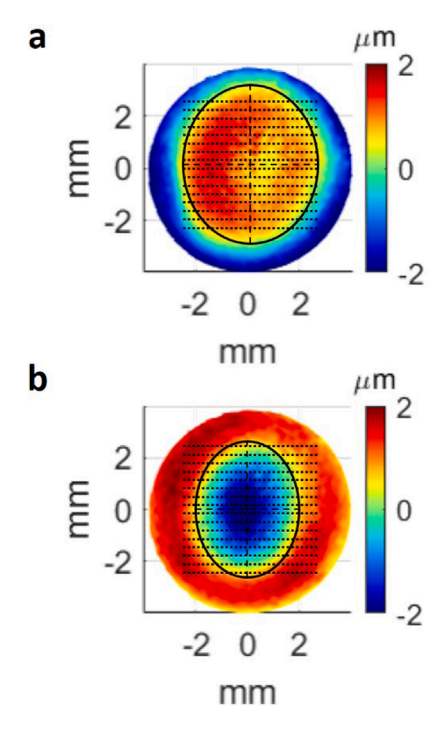


Fig. 6. Complex wave image for the anisotropic silicon-based phantom obtained from an axially-polarized MRE experiment at 900 Hz. (a) real part, (b) imaginary part. Elliptic boundaries of the wavefront are outlined as a solid black curve, semiaxes of the elliptic wavefront are indicated with dashed black lines while the direction of the fibers, being in-plane, is represented by dotted lines.

The same kind of results are presented for the anisotropic phantom in Fig. 9. The first column, corresponding to the axial MRE experiment at 900 Hz, shows an elongated ellipsoidal shape in the vertical direction, which is compatible with the fact the fibers for this phantom are oriented in the horizontal direction and the waves are predominantly radially converging to the center (top row: real part; bottom row: imaginary part). The second column contains the wave images in the θ direction resulting from the propagation of torsionally-polarized shear

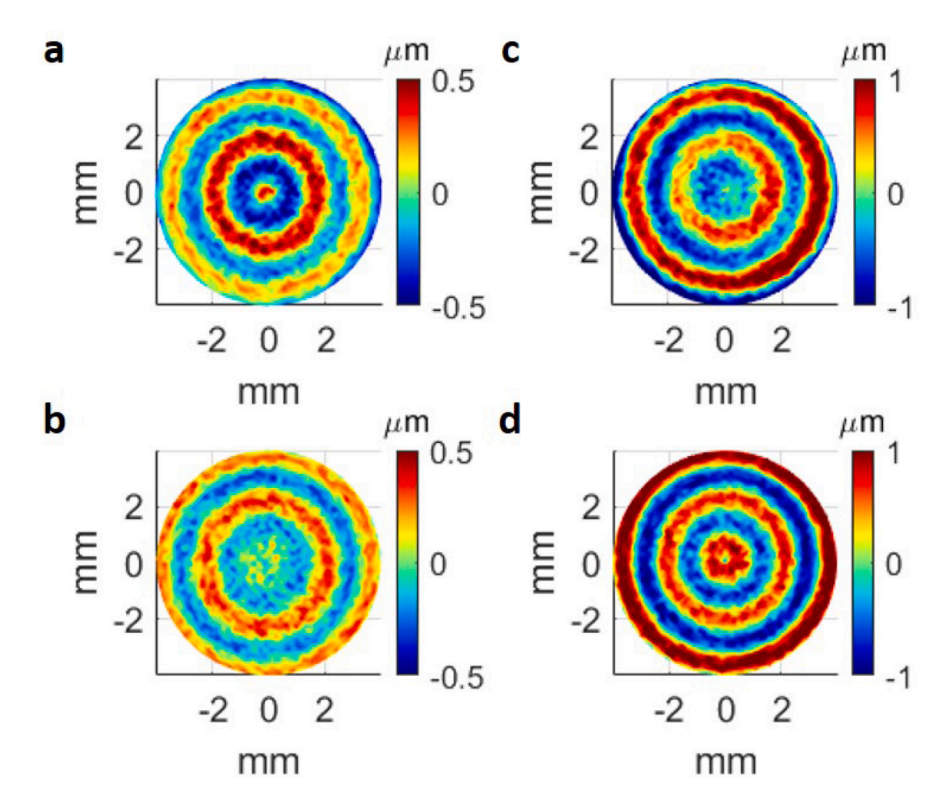


Fig. 7. Complex wave images from MRE experiment on homogeneous isotropic gelatin 5% w/v at 800 Hz. (a) and (b) show respectively the real (in phase) and the imaginary (out of phase) parts of the axial displacement maps obtained from an axially-polarized MRE experiment, while (c) and (d) correspond respectively to the real and imaginary parts of the θ displacement maps resulting from a torsionally-polarized MRE experiment.

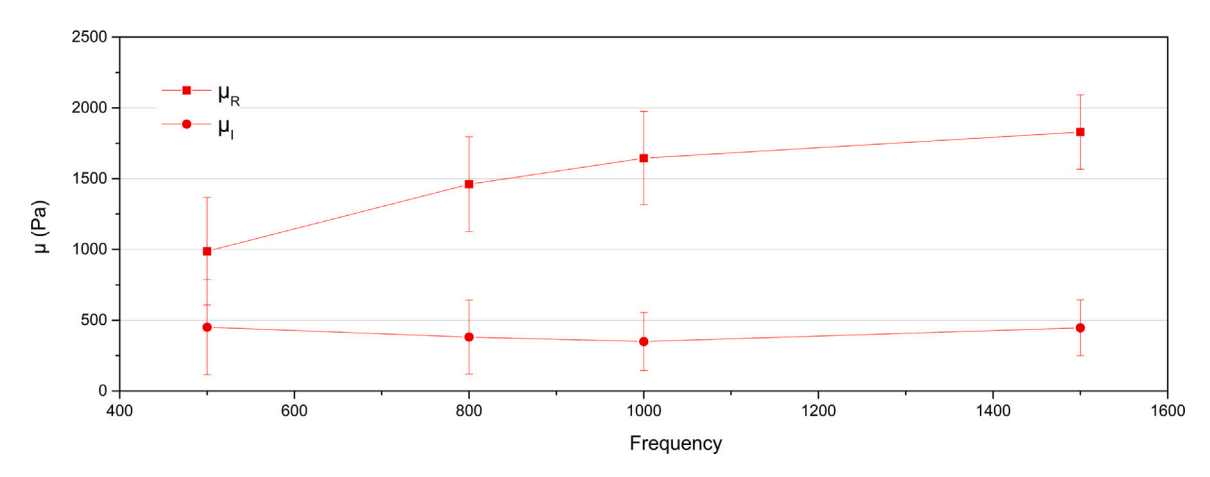


Fig. 8. Trends of the real (μ_R) and imaginary (μ_I) parts of the complex shear modulus as a function of frequency. Error bars representing one standard deviation of uncertainty are reported at each sampled excitation frequency.

waves through the silicone-based anisotropic phantom generated at 900 Hz by means of the stepper motor actuator (top row: real part; bottom row: imaginary part).

Shear modulus was computed upon the application of the direct inversion algorithm modified on the basis of the transformation elastography theory after the computation of the shear anisotropic ratio values of the axially-polarized complex wave images. The axial excitation response of the anisotropic phantom shows an increasing trend for both the real and imaginary parts of the shear modulus, with increasing excitation frequencies (Fig. 10). The values of shear modulus were also calculated under the assumption of isotropy by applying the conventional direct inversion algorithm; these last values (isotropic assumption) lie in between the curves corresponding to the shear moduli in the perpendicular and parallel direction with respect to the fibers (anisotropic assumption based on transformation elastography theory).

Shear modulus was computed by fitting the wave profiles with a closed form solution of the Bessel functions in a closed form expression and the corresponding results, in line with those obtained from the application of the direct inversion, are presented in Appendix A.

Axial and torsional wave images are also shown for the excised murine muscle sample in Fig. 11. The first column contains the wave images resulting from axially-polarized excitation at 800 Hz; again an elongated ellipse is visible in the images which shows a vertical preferential direction: this is consistent with the mouse fibers being horizontally arranged. The second column shows the wave images in the θ direction resulting from torsionally-polarized excitation.

Fig. 12 plots estimates of the shear storage and loss moduli for the excised mouse sample as a function of frequency, both under the isotropic and the anisotropic assumption as in Fig. 10 for the anisotropic phantom. The same results were obtained by applying

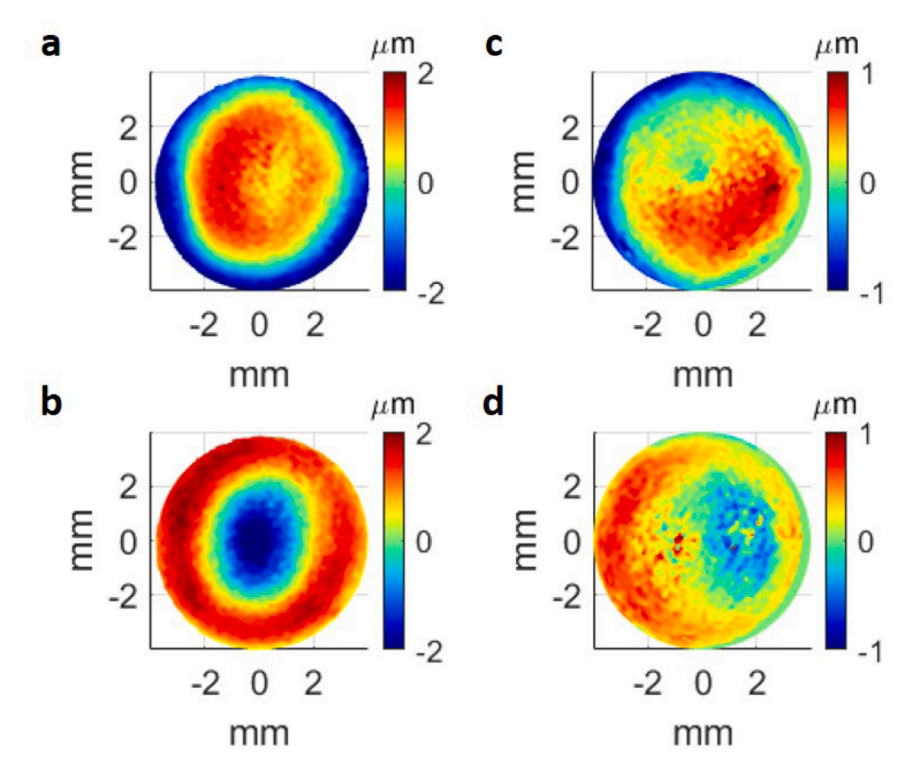


Fig. 9. Complex wave images from MRE experiment at 900 Hz on the anisotropic silicone-based phantom with in-plane fibers positioning. (a) and (b) show respectively the real (in phase) and the imaginary (out of phase) parts of the axial displacement maps obtained from an axially-polarized MRE experiment, while (c) and (d) correspond respectively to the real and imaginary parts of the θ displacement maps resulting from a torsionally-polarized MRE experiment.

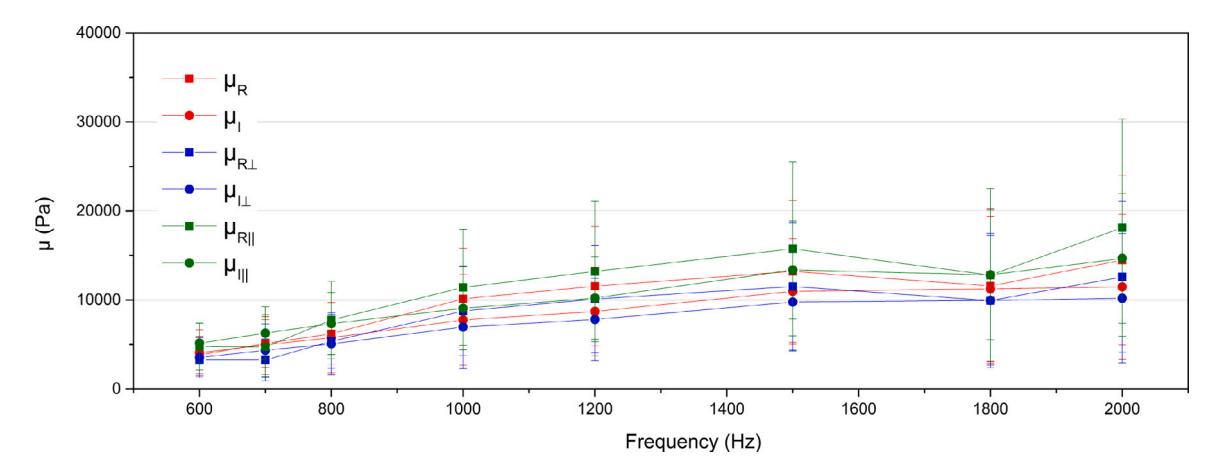


Fig. 10. Trends of the real and imaginary parts of the complex shear modulus as a function of frequency for the anisotropic phantom both under isotropic (μ_R and μ_I) and anisotropic ($\mu_{R\parallel}$, $\mu_{R\perp}$, $\mu_{I\parallel}$ and $\mu_{I\perp}$) assumptions. Error bars representing one standard deviation of uncertainty are reported at each sampled excitation frequency.

Bessel fit and the corresponding results, in line with those obtained from the application of the direct inversion, are presented in Appendix $^{\rm A}$

The present work was an experimental study following previous publications by the group that focused on the analysis of theoretical and simulated wave fields to provide insight into the expected experimental patterns, and confirmed the wave propagation behavior suggested by the implemented theoretical solutions (Guidetti et al., 2019; Guidetti and Royston, 2018, 2019a; Guidetti et al., 2019b). A direct future development of this work is the estimation of the shear moduli in the case of torsional actuation with in-plane fibers configuration, for which fast shear waves are generated. The Transformation Elastography technique could also be used in a future study to estimate the shear moduli in the case of torsional experiments, with the in-plane fiber configuration, for which fast shear waves are generated, given the addition of another parameter, the tensile anisotropic ratio, which

is defined as $\xi = \frac{E_{\parallel}}{E_{\perp}} - 1$, with E being the Young's modulus (Tweten et al., 2015). A limitation of this study is related to the restricted range of excitation frequencies for the MRE torsional experiment. This is due to the lower bandwidth of the stepper motor setup (~400 Hz resonant frequency with significant amplitude decay beyond that) compared to the piezoelectric setup where the resonance frequency is higher than the considered range of excitation frequencies.

4. Conclusion

The goal for this research study was to present an innovative fabrication method for a muscle mimicking anisotropic phantom that could be used as a standard for imaging studies of anisotropic materials, and to introduce a method for mechanical characterization of anisotropic samples by means of the MRE technique utilizing novel,

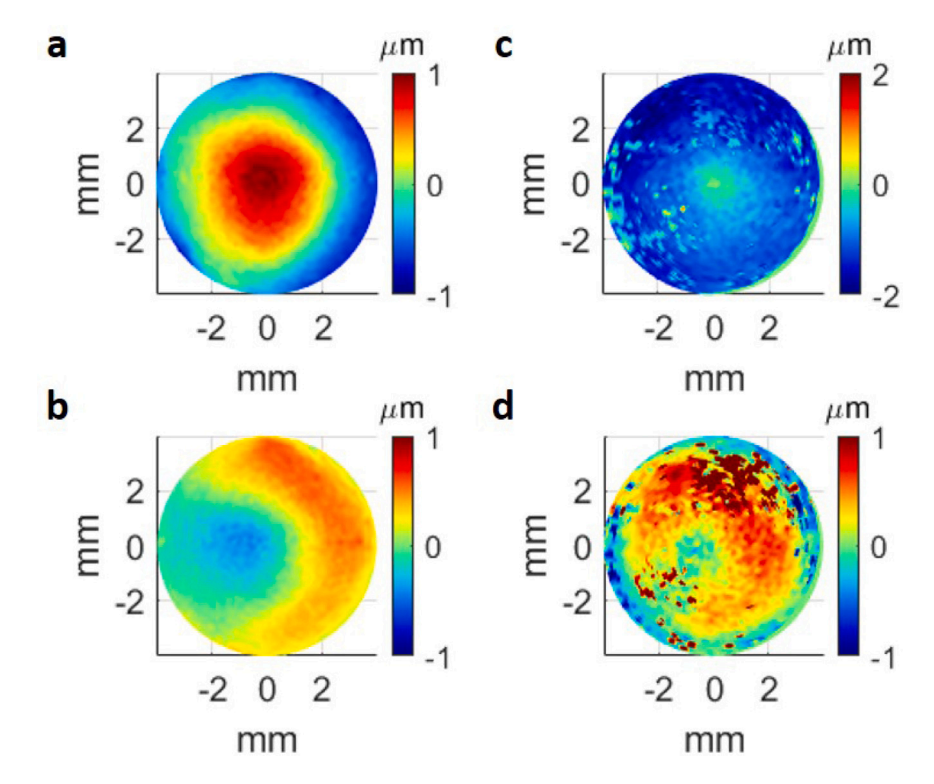


Fig. 11. Complex wave images from MRE experiment on the murine muscle sample constituted by calf and thigh muscles with in-plane fibers positioning. (a) and (b) show respectively the real (in phase) and the imaginary (out of phase) parts of the axial displacement maps obtained from an axially-polarized MRE experiment at 800 Hz, while (c) and (d) correspond respectively to the real and imaginary parts of the θ displacement maps resulting from a torsionally-polarized MRE experiment at 700 Hz.

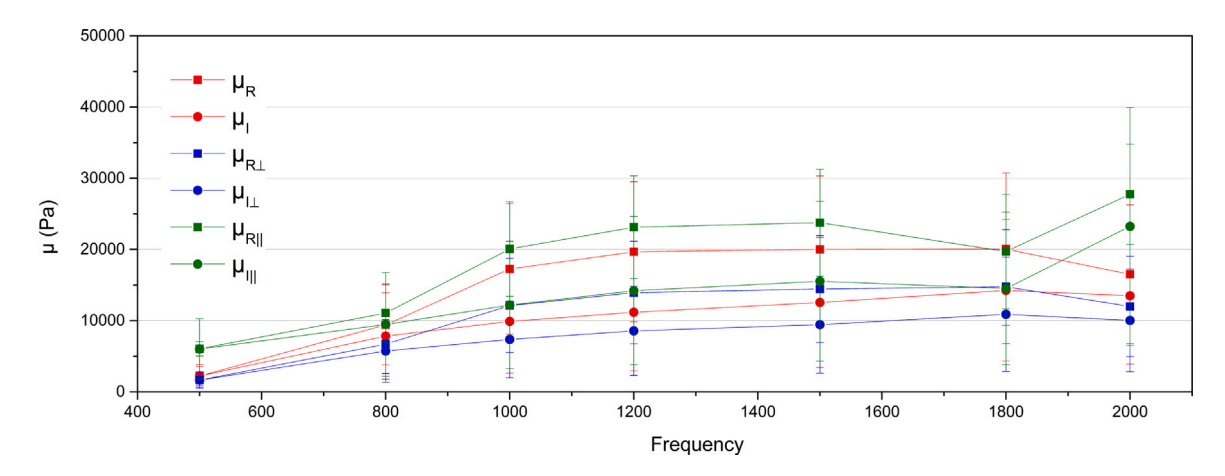


Fig. 12. Trends of the real and imaginary parts of the complex shear modulus as a function of frequency for the murine sample both under isotropic (μ_R and μ_I) and anisotropic ($\mu_{R\parallel}$, $\mu_{R\perp}$, $\mu_{I\parallel}$ and $\mu_{I\perp}$) assumptions. Error bars representing one standard deviation of uncertainty are reported at each sampled excitation frequency.

torsionally-polarized, radially-converging waves. Differences between the vertically- and torsionally-polarized actuation modalities are clear when displaying the respective wave images. The current torsional setup is frequency band limited relative to the axial setup. An improved design with a wider bandwidth is needed to fully utilize this approach in the tabletop MRI system.

CRediT authorship contribution statement

Martina Guidetti: Conceptualization, Methodology, Software, Investigation, Data curation, Writing - original draft, Writing - review & editing, Visualization, Validation, Project administration. Marco Andrea Zampini: Methodology, Software, Validation, Formal analysis, Writing - original draft, Writing - review & editing. Yizhou Jiang: Investigation, Formal analysis, Visualization, Writing - original draft,

Writing - review & editing. Chiara Gambacorta: Investigation. Joshua P. Smejkal: Investigation, Writing - original draft. Joseph Crutison: Investigation. Yayue Pan: Supervision, Writing - review & editing. Dieter Klatt: Supervision, Funding acquisition, Software, Writing - review & editing. Thomas J. Royston: Conceptualization, Supervision, Funding acquisition, Writing - review & editing, Project administration.

Declaration of competing interest

The authors declare that they have no known competing financial interests or personal relationships that could have appeared to influence the work reported in this paper.

Acknowledgments

The authors acknowledge funding from NSF, USA Grant No. 1852691 and NIH, USA Grant No. AR071162.

Appendix A. Supplementary data

Supplementary material related to this article can be found online at https://doi.org/10.1016/j.jmbbm.2021.104483.

References

- Ajmera, V.H., Liu, A., Singh, S., Yachoa, G., Ramey, M., Bhargava, M., Zamani, A., Lopez, S., Mangla, N., Bettencourt, R., et al., 2020. Clinical utility of an increase in magnetic resonance elastography in predicting fibrosis progression in nonalcoholic fatty liver disease. Hepatology 71 (3), 849–860.
- Amador, C., Urban, M.W., Chen, S., Chen, Q., An, K.-N., Greenleaf, J.F., 2011. Shear elastic modulus estimation from indentation and SDUV on gelatin phantoms. IEEE Trans. Biomed. Eng. 58 (6), 1706–1714.
- Anderson, A.T., Van Houten, E.E., McGarry, M.D., Paulsen, K.D., Holtrop, J.L., Sutton, B.P., Georgiadis, J.G., Johnson, C.L., 2016. Observation of direction-dependent mechanical properties in the human brain with multi-excitation MR elastography. J. Mech. Behav. Biomed. Mater. 59, 538–546.
- Basford, J.R., Jenkyn, T.R., An, K.-N., Ehman, R.L., Heers, G., Kaufman, K.R., 2002. Evaluation of healthy and diseased muscle with magnetic resonance elastography. Arch. Phys. Med. Rehabil. 83 (11), 1530–1536.
- Bensamoun, S.F., Ringleb, S.I., Chen, Q., Ehman, R.L., An, K.-N., Brennan, M., 2007. Thigh muscle stiffness assessed with magnetic resonance elastography in hyperthyroid patients before and after medical treatment. J. Magn. Reson. Imaging. 26 (3), 708–713.
- Botanlioglu, H., Kantarci, F., Kaynak, G., Unal, Y., Ertan, S., Aydingoz, O., Erginer, R., Unlu, M.C., Mihmanli, I., Babacan, M., 2013. Shear wave elastography properties of vastus lateralis and vastus medialis obliquus muscles in normal subjects and female patients with patellofemoral pain syndrome. Skelet. Radiol. 42 (5), 659–666.
- Braun, J., Tzschätzsch, H., Körting, C., Ariza de Schellenberger, A., Jenderka, M., Drießle, T., Ledwig, M., Sack, I., 2018. A compact 0.5 t MR elastography device and its application for studying viscoelasticity changes in biological tissues during progressive formalin fixation. Magn. Reson. Med. 79 (1), 470-478.
- Brinker, S.T., Kearney, S.P., Royston, T.J., Klatt, D., 2018. Simultaneous magnetic resonance and optical elastography acquisitions: Comparison of displacement images and shear modulus estimations using a single vibration source. J. Mech. Behav. Biomed. Mater. 84, 135–144.
- Brinker, S., Klatt, D., 2016. Demonstration of concurrent tensile testing and magnetic resonance elastography. J. Mech. Behav. Biomed. Mater. 63, 232–243.
- Cao, Y., Li, G.-Y., Zhang, X., Liu, Y.-L., 2017. Tissue-mimicking materials for elastography phantoms: A review. Extrem. Mech. Lett. 17, 62–70.
- Deffieux, T., Gennisson, J.-L., Bercoff, J., Tanter, M., 2011. On the effects of reflected waves in transient shear wave elastography. IEEE Trans. Ultrason. Ferroelectr. Freq. Control 58 (10), 2032–2035.
- Doyley, M.M., Bamber, J.C., Fuechsel, F., Bush, N.L., 2001. A freehand elastographic imaging approach for clinical breast imaging: system development and performance evaluation. Ultrasound Med. Biol. 27 (10), 1347–1357.
- Dutt, V., Kinnick, R.R., Muthupillai, R., Oliphant, T.E., Ehman, R.L., Greenleaf, J.F., 2000. Acoustic shear-wave imaging using echo ultrasound compared to magnetic resonance elastography. Ultrasound Med. Biol. 26 (3), 397–403.
- Fujii, T., 2002. PDMS-Based microfluidic devices for biomedical applications. Microelectron. Eng. 61, 907–914.
- Gal, O., 2020. fit_ellipse (www.mathworks.com/matlabcentral/fileexchange/3215-fit_ellipse), MATLAB Central File Exchange, (Retrieved December 21, 2020).
- Garmirian, L.P., Chin, A.B., Rutkove, S.B., 2009. Discriminating neurogenic from myopathic disease via measurement of muscle anisotropy. Muscle Nerve 39 (1), 16–24.
- Graff, K.F., 2012. Wave motion in elastic solids. Courier Corporation.
- Grosskopf, A.K., Truby, R.L., Kim, H., Perazzo, A., Lewis, J.A., Stone, H.A., 2018. Viscoplastic matrix materials for embedded 3D printing. ACS Appl. Mater. Interfaces 10 (27), 23353–23361.
- Guidetti, M., Caratelli, D., Royston, T.J., 2019b. Converging super-elliptic torsional shear waves in a bounded transverse isotropic viscoelastic material with nonhomogeneous outer boundary. J. Acoust. Soc. Am. 146 (5), EL451–EL457.
- Guidetti, M., Klatt, D., Royston, T.J., 2020. Transformation elastography: Converting anisotropy to isotropy. In: 2020 IEEE 17th International Symposium on Biomedical Imaging (ISBI). IEEE, pp. 1812–1815.
- Guidetti, M., Lorgna, G., Klatt, D., Vena, P., Royston, T.J., 2019. Anisotropic composite material phantom to improve skeletal muscle characterization using magnetic resonance elastography. J. Mech. Behav. Biomed. Mater. 89, 199–208.
- Guidetti, M., Royston, T.J., 2018. Analytical solution for converging elliptic shear wave in a bounded transverse isotropic viscoelastic material with nonhomogeneous outer boundary. J. Acoust. Soc. Am. 144 (4), 2312–2323.

- Guidetti, M., Royston, T.J., 2019a. Analytical solution for diverging elliptic shear wave in bounded and unbounded transverse isotropic viscoelastic material with nonhomogeneous inner boundary. J. Acoust. Soc. Am. 145 (1), EL59–EL65.
- Habe, T., Numano, T., Ito, D., Takamoto, K., Nishijo, H., Mizuhara, K., Ueki, T., Igarashi, K., 2020. Development of a suitable actuator for magnetic resonance elastography of the psoas major muscle. Appl. Magn. Reson. 1–12.
- Hall, T.J., Bilgen, M., Insana, M.F., Krouskop, T.A., 1997. Phantom materials for elastography. IEEE Trans. Ultrason. Ferroelectr. Freq. Control 44 (6), 1355–1365.
- Hamhaber, U., Grieshaber, F., Nagel, J., Klose, U., 2003. Comparison of quantitative shear wave MR-elastography with mechanical compression tests. Magn. Reson. Med. 49 (1), 71–77.
- Ipek-Ugay, S., Drießle, T., Ledwig, M., Guo, J., Hirsch, S., Sack, I., Braun, J., 2015.
 Tabletop magnetic resonance elastography for the measurement of viscoelastic parameters of small tissue samples. J. Magn. Reson. 251, 13–18.
- Jiang, Y., Cheng, M., Shahbazian-Yassar, R., Pan, Y., 2019. Direct ink writing of wearable thermoresponsive supercapacitors with rGO/CNT composite electrodes. Adv. Mater. Technol. 4 (12), 1900691.
- Kalra, P., Raterman, B., Mo, X., Kolipaka, A., 2019. Magnetic resonance elastography of brain: Comparison between anisotropic and isotropic stiffness and its correlation to age. Magn. Reson. Med. 82 (2), 671–679.
- Khan, A.A., Kearney, S.P., Royston, T.J., 2018. Finite element based optimization of human fingertip optical elastography. J. Eng. Sci. Med. Diagn. Ther. 1 (3), 031007.
- Kim, Y., Yuk, H., Zhao, R., Chester, S.A., Zhao, X., 2018. Printing ferromagnetic domains for untethered fast-transforming soft materials. Nature 558 (7709), 274–279.
- Klatt, D., Hamhaber, U., Asbach, P., Braun, J., Sack, I., 2007. Noninvasive assessment of the rheological behavior of human organs using multifrequency MR elastography: a study of brain and liver viscoelasticity. Phys. Med. Biol. 52 (24), 7281.
- Larin, K.V., Sampson, D.D., 2017. Optical coherence elastography–OCT at work in tissue biomechanics. Biomed. Opt. Express 8 (2), 1172–1202.
- Liang, X., Boppart, S.A., 2009. Biomechanical properties of in vivo human skin from dynamic optical coherence elastography. IEEE Trans. Biomed. Eng. 57 (4), 953–959.
- Lieber, R.L., Fridén, J., 2000. Functional and clinical significance of skeletal muscle architecture. Muscle Nerve 23 (11), 1647–1666.
- Madsen, E.L., Frank, G.R., 1997. Very low scatter liquid and solid tissue mimicking material for ultrasound phantoms and method of making the same. Google Patents, US Patent 5, 625, 137.
- Madsen, E.L., Hobson, M.A., Shi, H., Varghese, T., Frank, G.R., 2005. Tissue-mimicking agar/gelatin materials for use in heterogeneous elastography phantoms. Phys. Med. Biol. 50 (23), 5597.
- Manduca, A., Oliphant, T.E., Dresner, M.A., Mahowald, J., Kruse, S.A., Amromin, E., Felmlee, J.P., Greenleaf, J.F., Ehman, R.L., 2001. Magnetic resonance elastography: non-invasive mapping of tissue elasticity. Med. Image Anal. 5 (4), 237–254.
- M'barki, A., Bocquet, L., Stevenson, A., 2017. Linking rheology and printability for dense and strong ceramics by direct ink writing. Sci. Rep. 7 (1), 1-10.
- McCullough, M.B., Domire, Z.J., Reed, A.M., Amin, S., Ytterberg, S.R., Chen, Q., An, K.-N., 2011. Evaluation of muscles affected by myositis using magnetic resonance elastography. Muscle Nerve 43 (4), 585–590.
- Mori, Y., Tokura, H., Yoshikawa, M., 1997. Properties of hydrogels synthesized by freezing and thawing aqueous polyvinyl alcohol solutions and their applications. J. Mater. Sci. 32 (2), 491–496.
- Mun, H.S., Choi, S.H., Kook, S.H., Choi, Y., Jeong, W.K., Kim, Y., 2013. Validation of intra-and interobserver reproducibility of shearwave elastography: Phantom study. Ultrasonics 53 (5), 1039–1043.
- Muth, J.T., Vogt, D.M., Truby, R.L., Mengüç, Y., Kolesky, D.B., Wood, R.J., Lewis, J.A., 2014. Embedded 3D printing of strain sensors within highly stretchable elastomers. Adv. Mater. 26 (36), 6307–6312.
- Muthupillai, R., Lomas, D., Rossman, P., Greenleaf, J.F., Manduca, A., Ehman, R.L., 1995. Magnetic resonance elastography by direct visualization of propagating acoustic strain waves. Science 269 (5232), 1854–1857.
- Nguyen, K.-C.T., Le, L.H., Tran, T.N., Sacchi, M.D., Lou, E.H., 2014. Excitation of ultrasonic lamb waves using a phased array system with two array probes: Phantom and in vitro bone studies. Ultrasonics 54 (5), 1178–1185.
- Noor, N., Shapira, A., Edri, R., Gal, I., Wertheim, L., Dvir, T., 2019. 3D Printing of personalized thick and perfusable cardiac patches and hearts. Adv. Sci. 1900344.
- Oudry, J., Bastard, C., Miette, V., Willinger, R., Sandrin, L., 2009. Copolymer-in-oil phantom materials for elastography. Ultrasound Med. Biol. 35 (7), 1185–1197.
- Parker, K., Huang, S., Musulin, R., Lerner, R., 1990. Tissue response to mechanical vibrations for "sonoelasticity imaging". Ultrasound Med. Biol. 16 (3), 241–246.
- Pavan, T.Z., Madsen, E.L., Frank, G.R., Carneiro, A.A.O., Hall, T.J., 2010. Nonlinear elastic behavior of phantom materials for elastography. Phys. Med. Biol. 55 (9), 2679.
- Plewes, D.B., Bishop, J., Samani, A., Sciarretta, J., 2000. Visualization and quantification of breast cancer biomechanical properties with magnetic resonance elastography. Phys. Med. Biol. 45 (6), 1591.
- Qin, E.C., Jugé, L., Lambert, S.A., Paradis, V., Sinkus, R., Bilston, L.E., 2014. In vivo anisotropic mechanical properties of dystrophic skeletal muscles measured by anisotropic MR elastographic imaging: the mdx mouse model of muscular dystrophy. Radiology 273 (3), 726–735.

- Quan, K., Christison, G., MacKenzie, H., Hodgson, P., 1993. Glucose determination by a pulsed photoacoustic technique: an experimental study using a gelatin-based tissue phantom. Phys. Med. Biol. 38 (12), 1911.
- Ringleb, S.I., Bensamoun, S.F., Chen, Q., Manduca, A., An, K.-N., Ehman, R.L., 2007.
 Applications of magnetic resonance elastography to healthy and pathologic skeletal muscle. J. Magn. Reson. Imaging 25 (2), 301–309.
- Ringleb, S.I., Chen, Q., Lake, D.S., Manduca, A., Ehman, R.L., An, K.-N., 2005. Quantitative shear wave magnetic resonance elastography: comparison to a dynamic shear material test. Magn. Reson. Med. 53 (5), 1197–1201.
- Sack, I., Jöhrens, K., Würfel, J., Braun, J., 2013. Structure-sensitive elastography: on the viscoelastic powerlaw behavior of in vivo human tissue in health and disease. Soft Matter 9 (24), 5672–5680.
- Sarvazyan, A., J Hall, T., W Urban, M., Fatemi, M., R Aglyamov, S., S Garra, B., 2011.
 An overview of elastography-an emerging branch of medical imaging. Curr. Med. Imaging Rev. 7 (4), 255–282.
- Schmidt, J., Tweten, D., Badachhape, A., Reiter, A., Okamoto, R., Garbow, J., Bayly, P., 2018. Measurement of anisotropic mechanical properties in porcine brain white matter ex vivo using magnetic resonance elastography. J. Mech. Behav. Biomed. Mater. 79, 30–37.
- Smay, J.E., Cesarano, J., Lewis, J.A., 2002. Colloidal inks for directed assembly of 3-d periodic structures. Langmuir 18 (14), 5429–5437.
- Truby, R.L., Wehner, M., Grosskopf, A.K., Vogt, D.M., Uzel, S.G., Wood, R.J., Lewis, J.A., 2018. Soft somatosensitive actuators via embedded 3D printing. Adv. Mater. 30 (15), 1706383.

- Tweten, D.J., Okamoto, R.J., Schmidt, J.L., Garbow, J.R., Bayly, P.V., 2015. Estimation of material parameters from slow and fast shear waves in an incompressible, transversely isotropic material. J. Biomech. 48 (15), 4002–4009.
- Von Gierke, H.E., Oestreicher, H.L., Franke, E.K., Parrack, H.O., von Wittern, W.W., 1952. Physics of vibrations in living tissues. J. Appl. Physiol. 4 (12), 886–900.
- Wang, M., Byram, B., Palmeri, M., Rouze, N., Nightingale, K., 2013. Imaging transverse isotropic properties of muscle by monitoring acoustic radiation force induced shear waves using a 2-d matrix ultrasound array. IEEE Trans. Med. Imaging 32 (9), 1671–1684.
- Yamakoshi, Y., Sato, J., Sato, T., 1990. Ultrasonic imaging of internal vibration of soft tissue under forced vibration. IEEE Trans. Ultrason. Ferroelectr. Freq. Control 37 (2), 45–53.
- Yasar, T.K., Royston, T.J., Magin, R.L., 2013. Wideband MR elastography for viscoelasticity model identification. Magn. Reson. Med. 70 (2), 479–489.
- Zell, K., Sperl, J., Vogel, M., Niessner, R., Haisch, C., 2007. Acoustical properties of selected tissue phantom materials for ultrasound imaging. Phys. Med. Biol. 52 (20), N475
- Zhao, J., He, N., 2020. A mini-review of embedded 3D printing: supporting media and strategies. J. Mater. Chem. B 8 (46), 10474–10486.
- Zhao, J., Hussain, M., Wang, M., Li, Z., He, N., 2020. Embedded 3D printing of multi-internal surfaces of hydrogels. Addit. Manuf. 32, 101097.